NiO Nanosheet Array Integrated Monoliths for Low Temperature Catalytic Propane Oxidation: A Study on the Promotion Effect of Ce Doping

Wenxiang Tang[a,b], Xingxu Lu[b], Junfei Weng[b] and Pu-Xian Gao[b]*

[a] School of Chemical Engineering, Sichuan University, Chengdu, Sichuan, 610025, P. R. China

[b] Department of Materials Science and Engineering & Institute of Materials Science, University of Connecticut, Storrs, CT 06269-3136, USA

*E-mail correspondence: puxian.gao@uconn.edu

Abstract:

Constructing robust catalysts by growing nanostructure arrays directly onto honeycomb monoliths is a promising technology for fabricating highly active reactors with low materials usage and cost-effectiveness. In this study, catalytically active NiO nanosheet arrays were uniformly grown onto the channel surfaces of cordierite honeycombs to form monolithic catalysts with ultra-low loading. Ce doping was found to significantly enhance the catalytic propane oxidation performance of pristine NiO nanosheet arrays. With a Ce doping of ~4 wt.% in NiO, a conversion of 90% propane oxidation into CO_2 was achieved at 440 °C, a ~40 ^{o}C decrease compared to the pristine NiO under a space velocity of 24,000 h^{-1}. With the promoting effect of Ce, the Ce-doped NiO nanosheet arrays exhibited a much better thermal stability, with only 1.1% loss of conversion after a 48h operation at 425 °C, in comparison with a 21.5% loss over the pristine NiO catalyst.

Key words:

NiO nanosheet array, monolithic catalyst, Ce doping, propane oxidation, thermal stability

1. Introduction

Ceramic honeycomb monoliths integrated with active components on their channeled surfaces is a major type of catalytic reactors for various industrial and transportation applications such as chemical processing, hydrocarbon combustion converter, catalyzed diesel particulate filter (C-DPF), air purifier and water treatment [1-4]. These ceramic-based monolithic reactors hold many advantages such as low thermal expansion coefficient, high thermal resistance, low pressure drop, and good mechanical stability [2, 5, 6]. Generally, ceramic monolith reactors integrate composition- and thickness-controlled coatings onto the monolithic channel surfaces by virtue of a washcoating process in industry. The coating process usually starts with the preparation of a slurry of mixing support (Al_2O_3, SiO_2, TiO_2), active precursors (active metal/oxide nanoparticles or related salts), and some additives, and then proceeds with a washcoating step. The washcoating process includes a few steps from filling, sweeping, drying, to thermal annealing, with several repeated washcoating procedures to ensure the loading and uniformity of coverage. However, a few challenges remain in this traditional washcoating process, [7-10] including (1) the materials utilization efficiency could be compromised due to the poor mass transfer in the washcoat layers; (2) nanostructure-derived activity might be lost due to some irreversible nanostructures damages during the washcoat slurry deposition process; (3) internal mass transfer in either dense or irregularly porous washcoat may be limited by the large coating thickness; (4) low mechanical stability is another critical issue under high space velocity, thermal shock operation, and mechanical vibration. Recently, a new configuration of monolithic catalysts by directly integrating functional nanostructure arrays (nanoarrays) onto ceramic and metallic honeycomb monoliths [11-19], which provides a new type of monolithic reactors for energy and environmental applications.

Catalytic combustion of hydrocarbons (HCs) is one of the most effective technology solutions for controlling the HC emissions. Up to now, supported platinum group metals (PGM) based washcoat monolithic catalysts have been applied in engine exhaust aftertreatment, such as three-way catalyst (TWC) and diesel oxidation catalyst (DOC) in automobiles [20-23]. However, these PGM based catalysts still face challenges including high pricing and drawbacks such as volatility, sintering of PGM and loss of active sites, and poisoning tendency under atmosphere involving SO_2 and

NO_x [20, 24-26]. Therefore, it is highly desirable to develop cost-competitive alternatives for replacing the prohibitive PGM based catalysts. In the past few decades, low-cost metal oxides such as MnO_x, Co_3O_4, CuO, NiO, and perovskite ABO_3 [27-32] have been found to be highly active for the total oxidation of hydrocarbons. Centering around these active metal oxides, extensive efforts have been made to improve their catalytic performance, specifically using typical strategies such as nanostructure assembly, morphology tuning, and composite formation. It is noted that most of these studies have been focused on the powder-form catalysts, which have been prevented from practical applications by some processing hurdles. For example, using washcoating process, the individual nanostructure-derived high performance may be compromised due to the loss of the active surfaces with the randomly assembling process. As a result, developing a novel integration technology is highly desirable for assembling the nanostructured metal oxides with the most of the active surface exposed possible.

Recently, using scalable solution-based hydrothermal method, we have successfully *in situ* grown various arrays of metal oxide nanostructures such as nanoplates, nanorods, nanowires and nanotubes onto three-dimensional (3D) channeled honeycomb substrates [11-14, 16-19, 33-39]. In this study, we successfully grow NiO nanosheet arrays onto 3D channel surfaces of cordierite honeycomb to form a new type of NiO nanoarray based monolithic catalysts using a low-temperature (~95ºC) hydrothermal strategy. It is noted that NiO has been used in various catalytic reactions such as CO oxidation [40, 41], VOCs combustion [42-45], ozone decomposition [46, 47], N_2O decomposition [48, 49], SCR reaction [50, 51], water oxidation/splitting [52-54], and methane reforming/partial oxidation [55-58]. Here in this study, we also demonstrated that these PGM-free NiO nanosheet array integrated cordierite honeycomb monoliths perform effectively for catalytic propane oxidation at low temperature with a ultra-low material usage. With doping of Ce, the nanoarray catalyst performance can be further improved with well-retained array structures. The ordered array structure and uniform distribution enabled effective mass transport and improved reaction kinetics [11].

2. Experimental

2.1 Materials preparation

The commercial cordierite ($(Mg, Fe)_2Al_3(Si_5AlO_{18})$) honeycomb (600 cell per

square inch (cpsi), Corning Inc.) was used as a substrate to grow NiO nanosheet arrays onto the channel surfaces. Before the growth, the honeycomb substrate was sonicated and washed with ethanol and water to remove residual contaminants on the surfaces. A low-temperature hydrothermal process [11, 12, 14, 59] was employed to grow NiO nanosheet array. Firstly, nickel nitrate hexahydrate ($Ni(NO_3)_2•6H_2O$) and hexamethylenetetramine ($(CH_2)_6N_4$) were dissolved in 15 ml deionized water to generate transparent green reaction solution, with the concentration controlled at 5 and 25 mmol respectively. Then a honeycomb substrate with a size of 1cm × 1 cm × 2 cm was immersed into the solution, followed by the sonication to remove the residual gas bubbles from the substrate surface. The hydrothermal reaction was operated at 95 °C for 6 h, and the obtained sample was washed with water and ethanol, and then dried at 90 °C overnight. The final NiO array catalyst was obtained by annealing the as-prepared sample at 500 °C for 2 h. The Ce doping was carried out by adding cerium(III) nitrate hexahydrate ($Ce(NO_3)_3•6H_2O$) into the reaction solution before the hydrothermal process, with a varied concentration of $Ce(NO_3)_3•6H_2O$ controlled at 0.1, 0.2, 0.4, and 1 mmol. The as-synthesized samples were labeled as 0.1Ce-5NiO, 0.2Ce-5NiO, 0.4Ce-5NiO, and 1Ce-5NiO, respectively.

2.2 Materials characterization

A FEI Teneo LVSEM scanning electron microscope (SEM) attached with an energy dispersive X-ray (EDX) spectrometer was used to investigate the morphology and composition of the prepared samples. The structures of selected samples were characterized by a FEI Talos scanning transmission electron microscope (S/TEM) with an accelerating voltage of 200 kV. For STEM sample preparation, the array structure was scraped from cordierite honeycomb, and then dispersed in ethanol, followed by drop-cast deposition on a Cu grid with carbon film. The crystal structures were characterized using a D5005 X-ray diffractometer (BRUKER AXS) with Cu-Kα radiation in a diffraction angle (2θ) range of 25-70°. An ASAP 2020 automatic surface analyzer (Micromeritics Instrument Co.) was used to do N_2 adsorption-desorption analysis for acquiring samples' surface and porosity characteristics, such as Brunauer-Emmett-Teller (BET) surface area and the pore size distributions. Hydrogen temperature programmed reduction (H_2-TPR) analysis was carried out on a ChemiSorb 2720 automated catalyst characterization system

(Micromeritics Instrument Co.). In each run, one piece of catalyst monolith with 36 channels (1 cm long) was loaded in a U-shape quartz tube, which was heated to 700 °C with a ramp rate of 10 °C•min^{-1} under a reduced gas flow (4% H_2 balanced with Ar, 25mL•min^{-1}). X-ray photoelectron spectroscopy (XPS) was used for characterizing the surface composition and valence state distribution of samples using a PHI Quantera SXM spectrometer with multi-probes and Al-Kα radiation source. All peaks were calibrated with C 1s photoelectron line at 284.6 eV.

2.3 Catalytic performance evaluation

Propane oxidation was used as a probe reaction to investigate the catalytic performance of as-synthesized samples. In this study, catalytic propane oxidation was operated on a BenchCAT system (Altamira Instruments Inc.), and the feed reactant gas was composed of 0.3% C_3H_8, 10% O_2, and 89.7% N_2 with a total flow rate of 100 ml min^{-1}. The gas species such as CO_2, CO, and C_3H_8 in the exhaust stream were separated and detected by an Agilent Micro-GC equipped with a HP-PLOT Q and a TCD detector. The monolithic catalyst used in each run is of a size of 5 mm × 5 mm × 10 mm, about 0.1g, and 25 channels, with a space velocity (SV) controlled at 24,000 h^{-1}. Due to the ultra-low loading of active NiO catalysts, i.e., 6.3% - 7.1% including cordierite substrate, the actual materials usage in the tests was only about 6.5 mg.

3. Results and discussion

3.1 Catalytic combustion of propane

Propane is highly stable with a total non-catalytic conversion below 5% even at 500 °C. Fig. 1a presents the catalytic conversion of propane oxidation over the NiO based nanosheet array catalysts as a function of reaction temperature. The T_{10}, T_{50} and T_{90} (the reaction temperatures at which 10, 50 and 90% propane oxidation were completed, respectively) are summarized in Table 1. For pure NiO nanoarray monolith, the T_{10}, T_{50}, and T_{90} are 350, 422, and 481 °C, respectively. It is worth noting that the material usage of NiO is ~ 6.9 mg/0.25 mL (27.6 g/L), at least 5 times lower than that of traditional powder-washcoat catalyst (>150 g/L). Furthermore, this PGM free NiO catalyst still has a good potential to improve its performance. With cerium dopant, all the catalysts with a similar material loading demonstrated better propane oxidation activities, indicating a promotion effect of Ce on the NiO catalyst.

For instance, the T_{10}, T_{50} and T_{90} over 0.2Ce-5NiO are 323, 395, and 440 °C, which are 27, 27, and 41 °C lower than those of the pristine NiO catalysts, respectively. With a higher doping amount, both 0.4Ce-5NiO and 1Ce-5NiO samples showed a decline of the catalytic activity. These results proved the Ce can significantly improve the catalytic performance of NiO nanoarray monolithic catalyst but appropriate doping concentration is needed.

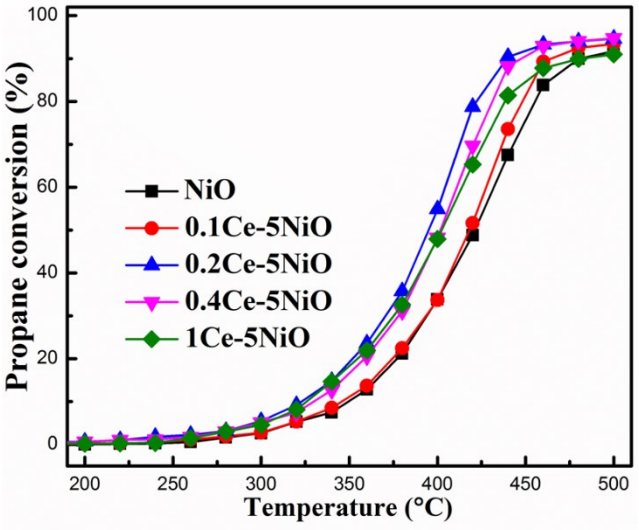

Figure 1. Catalytic combustion of C_3H_8 over Ce doped NiO nanosheet array monolithic catalysts as a function of temperature.

It is known that the catalytic combustion of most of hydrocarbons including propane follows the first-order reaction kinetic mechanism under oxygen-rich condition [60, 61]. The reaction rate in total propane oxidation can be expressed as $r_{C_3H_8} = (A\exp(\frac{-E_a}{RT}))\, C_{C_3H_8}^{a} C_{O_2}^{b}$, where $r_{C_3H_8}$ is reaction rate (mol g_{cat}^{-1} s^{-1}), A is the pre-exponential factor, E_a is the apparent activation energy (kJ mol^{-1}), and C_{C3H8} and C_{O2} are the concentrations of C_3H_8 and O_2, respectively. When the propane conversion is lower than 15%, the reactant feed gas can be considered to be constant so that the equation can be simplified by taking the logarithm. The new equation will be $\ln r_{C_3H_8} = -E_a/(RT) + C$ (C is a constant number) where the activation energy (E_a) can be calculated from the slope of the Arrhenius plots of $\ln r_{C_3H_8}$ as a function of inverse of absolute temperature (1/T), as shown in Figure 2. An excellent linear relationship was revealed on the $\ln r_{C_3H_8}$ vs. 1/T with its correlation coefficient (R^2) close to 1.0 as listed in Table 1. The E_a value of 0.2Ce-NiO (68.7 kJ mol^{-1}) is the lowest one, confirming the faster surface reaction kinetics in Ce doped NiO nanoarrays.

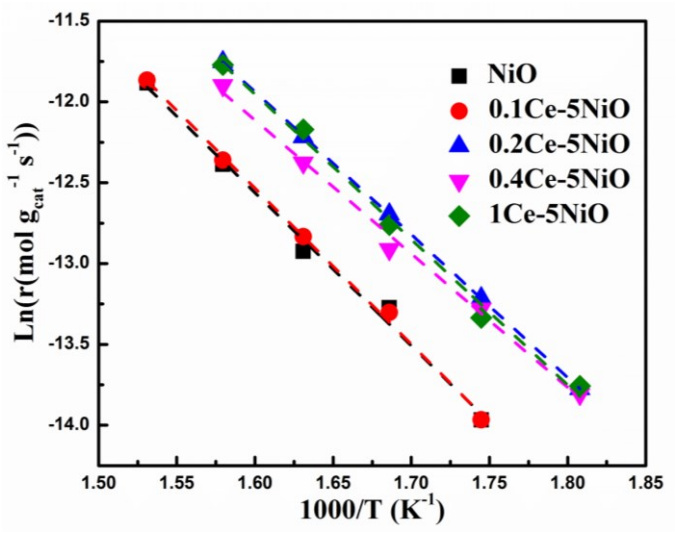

Figure 2. Arrhenius plots (ln(r mol g_{cat}^{-1} s^{-1}) vs. 1000/T (K^{-1})) for the catalytic combustion of C_3H_8 over the Ce doped NiO nanoarray catalysts.

Figure 3a shows the catalytic performance of pristine NiO and Ce-doped nanoarray monolithic catalysts comparatively. The enhancement through doping cerium is evident with the significantly reduced temperature for propane oxidation conversion. Moreover, the promoting effect has also been confirmed by running the time dependent on-stream experiment at 425 °C. For the pristine NiO catalyst, the initial conversion of 79.9% would decrease to 58.4% after one hour running, and decrease to 21.5% after 48 hour running, indicating its poor stability. However, the Ce doped NiO catalyst (0.2Ce-5NiO) decreases by only 1.1%, which means cerium doping can improve the catalyst durability significantly besides promoting its catalytic performance.

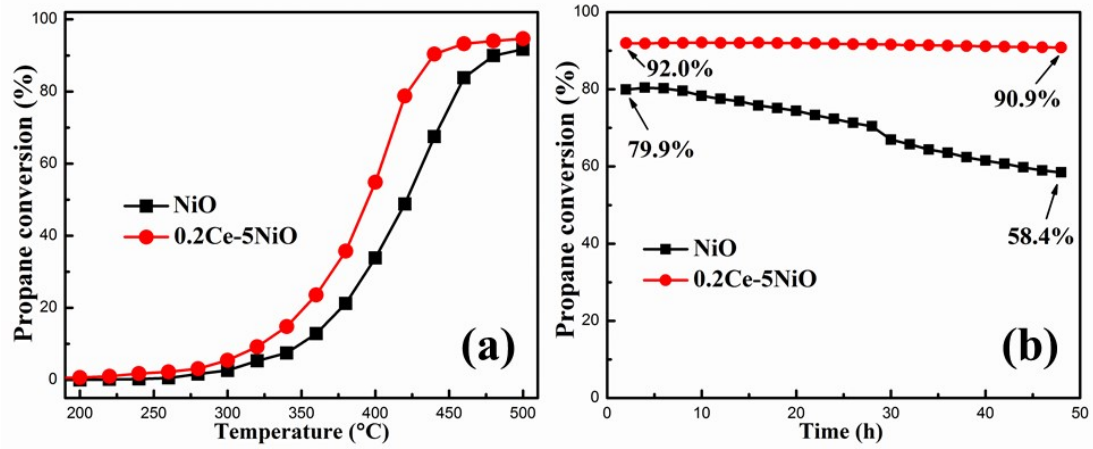

Figure 3. Comparison of pristine NiO and 0.2Ce-NiO nanoarray monolithic catalysts: (a) temperature dependent catalytic combustion of C_3H_8; (b) time dependent on-stream C_3H_8 oxidation conversion at 425 °C. C_3H_8 concentration = 0.3%, O_2 = 10%,

N_2 balance, and SV = 24 000 h^{-1}.

Table 1. Physical properties, catalytic activities, and activated energy of Ce doped NiO nanoarray catalysts.

samples	Textural properties			Active catalyst weight (mg)	Catalytic activities			Activation energy		
	Loading ratio (wt %)	Surface area[1] (m^2 g^{-1})	Pore diameter (nm)		T10 (°C)	T50 (°C)	T90 (°C)	slope	Adj. r^2	E_a (kJ mol^{-1})
NiO	6.9	4.6	21.7	6.9	350	422	481	-9.46	0.991	78.7
0.1Ce-5NiO	7.1	4.1	30.9	7.1	346	418	466	-9.64	0.997	80.1
0.2Ce-5NiO	6.7	4.2	31.6	6.7	323	395	440	-8.26	1.000	68.7
0.4Ce-5NiO	6.7	4.0	36.6	6.7	326	402	448	-8.84	0.993	73.5
1Ce-5NiO	6.3	5.1	17.6	6.3	330	402	485	-8.99	0.992	74.7

3.2 Morphologies and microstructures

Fig. 4 displays the top-view SEM images of the as-prepared NiO based monolithic catalyst with different cerium doping contents. As shown in Fig. 4a, some macropores can be observed on the surface of blank cordierite. With the simple hydrothermal process, the uniform NiO nanosheet array can be *in situ* grown on the channel surface of cordierite honeycomb. It is observed that the NiO nanosheets are interconnected to form well-distributed pore-network of sub-micrometer size. These special open spaces could provide an excellent mass-diffusion environment for catalytic oxidation process. After cerium doping into the NiO nanoarray, no obvious morphology change was observed until the ratio of Ce/Ni reaches 20%. For the 1Ce-5Ni sample, a number of cracks are revealed in Fig. 4f, despite the nanosheet unit being kept well. Moreover, the pore-space became smaller among interconnected nanosheets with increasing cerium doping concentration, suggesting the grown NiO nanoarray density was influenced by the doping of cerium.

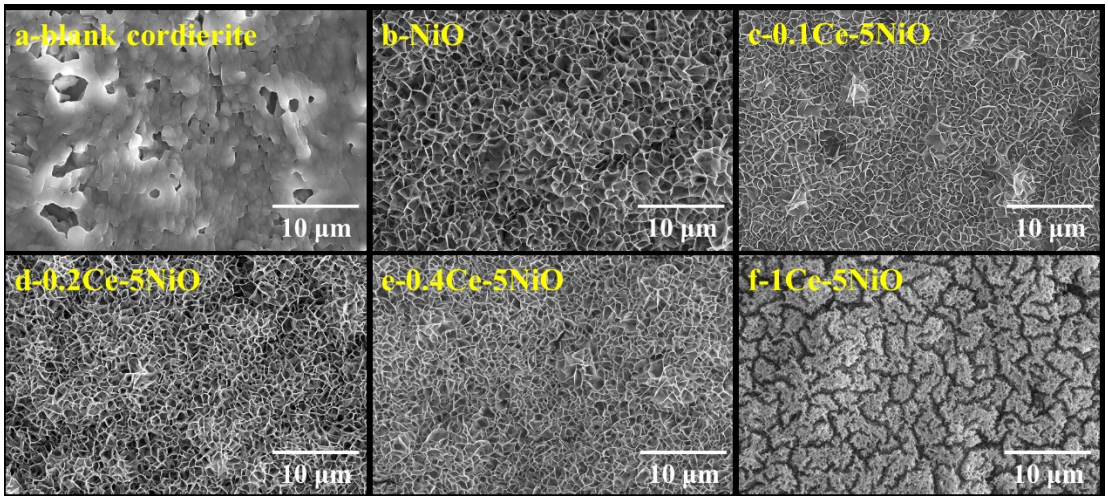

Figure 4. SEM images of the blank cordierite and the Ce doped NiO array monolithic catalysts.

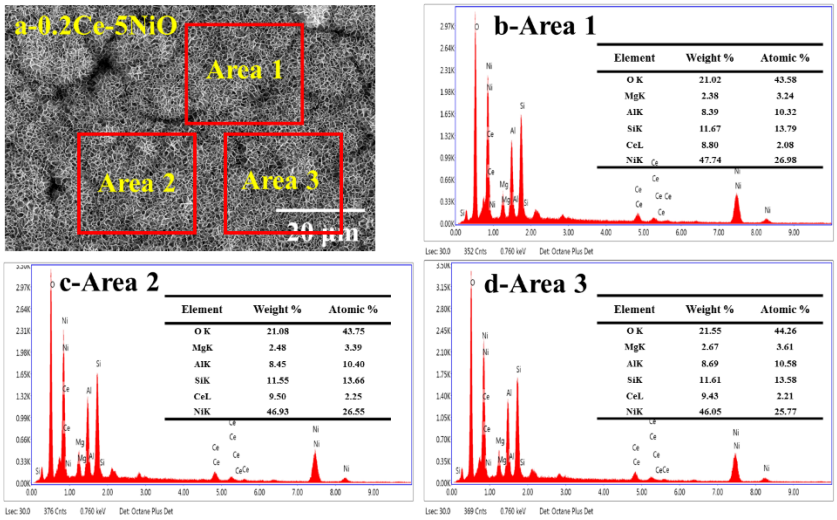

Figure 5. SEM-EDX data of three selected areas on sample 0.2Ce-5NiO.

The 0.2Ce-5Ni catalyst of the best catalytic performance was selected for energy dispersive X-ray spectroscopy (EDXS) elemental analysis. As shown in Fig. 5, three areas on the array nanostructure were chosen for the EDXS analyses. The obtained EDX spectra have similar peaks assigned to the elements of Mg, Al, Si, Ni, Ce and O, with the Mg, Al, and Si belonging to the cordierite substance, while Ni and Ce ascribed to nanosheet array, respectively. The elemental contents calculated from the spectrum peaks over these three areas were very close, further indicating the uniform distribution of Ce-Ni nanostructure array across the honeycomb channel surfaces. Meanwhile, the Ce/Ni ratio is about 8-9%, which is higher than the precursor amount used in the synthetic process, indicating the diverse hydrolysis reactions of Ce and Ni ions. Fig. 6 shows the typical cross-sectional view SEM images and the corresponding

EDXS elemental mappings of the 0.2Ce-5Ni sample. Fig. 6a demonstrated the nanosheet array layer with a thickness of 5 μm was well integrated onto the ceramic surface, where the bottom cordierite substrate was confirmed in the elemental mappings shown inFigs. 6d, e, f, and i. Additionally, the uniform Ce and Ni elemental distribution on the selected cross-sectional area further confirmed that the cerium was highly dispersed on the NiO nanostructures.

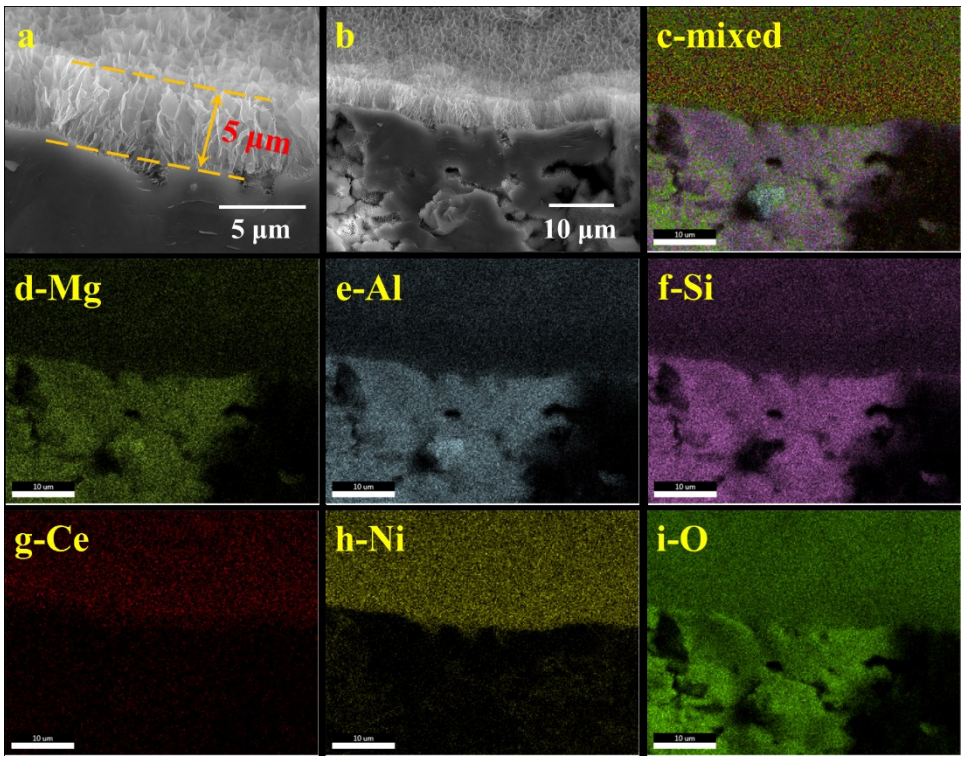

Figure 6. (a-b) A typical cross-sectional view SEM image and (c-i) elemental distribution of a cross-sectional view of sample 0.2Ce-5NiO.

The detailed structures of each nanosheet in 0.2Ce-5Ni array were further investigated by STEM analyses. As shown in Figs. 7a-b, the sheet morphology of NiO array unit was confirmed. It is noted that the sheet nanostructure is composed of many nanoparticles interconnected with each other to form a mesoporous 2D architecture. The irregular pores with a size ranging from 5 to 25 nm can be attributed to the release of CO_x (CO or CO_2) and H_2O products during the decomposition of nickel precursors such as hydrate and carbonate. Such an interconnected mesoporous network is beneficial for the formation of surface defects and provides an excellent mass transfer environment for catalytic reactions. The corresponding high resolution TEM (HRTEM) image in Fig. 7c exhibits the typical lattice fringe of a spacing of 0.15 nm, matching to the {220} crystal planes of cubic structured NiO. With cerium

doping, the sheet morphology is retained very well and the porous network becomes denser as revealed in Figs. 7d and f. The pore size distribution becomes wider, with the large pores > 50 nm while small pores <10 nm. The lattice fringe observed on the Ce doped NiO is of a spacing of 0.24 nm that matches the {111} crystal planes of cubic structured NiO. The high-resolution elemental maps of the 0.2Ce-5Ni sample in Fig. 8 reveal that Ce, Ni and O are uniformly distributed within the nanosheet structure, further demonstrating the successful Ce doping in the sample 0.2Ce-5Ni. The EDXS analysis shows the atomic ratio of Ce/Ni is about 7.6%, consistent with the SEM-mapping results in Fig. 5.

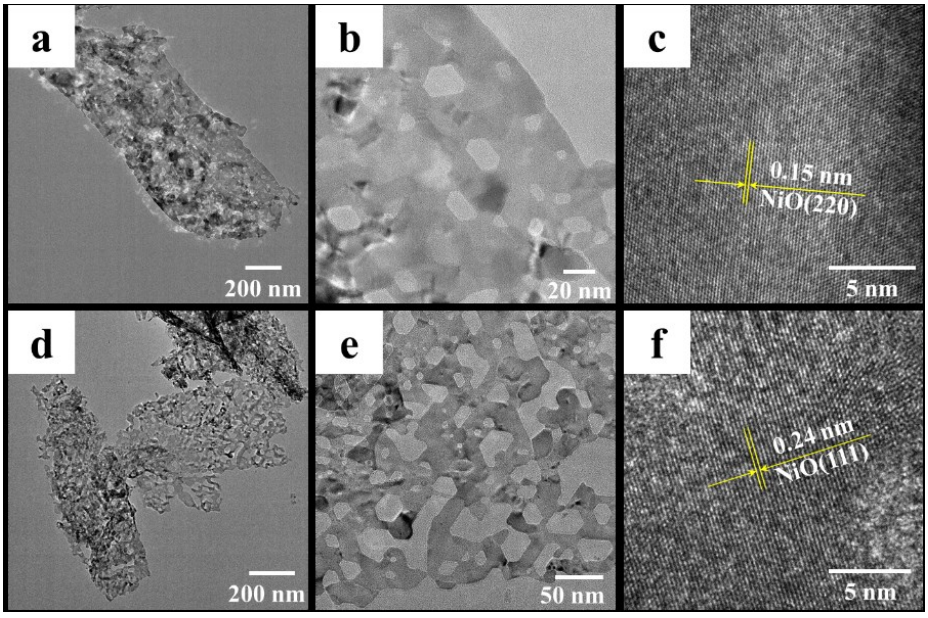

Figure 7. TEM and HR-TEM images of the investigated sample NiO (a-c) and 0.2Ce-5NiO (d-f).

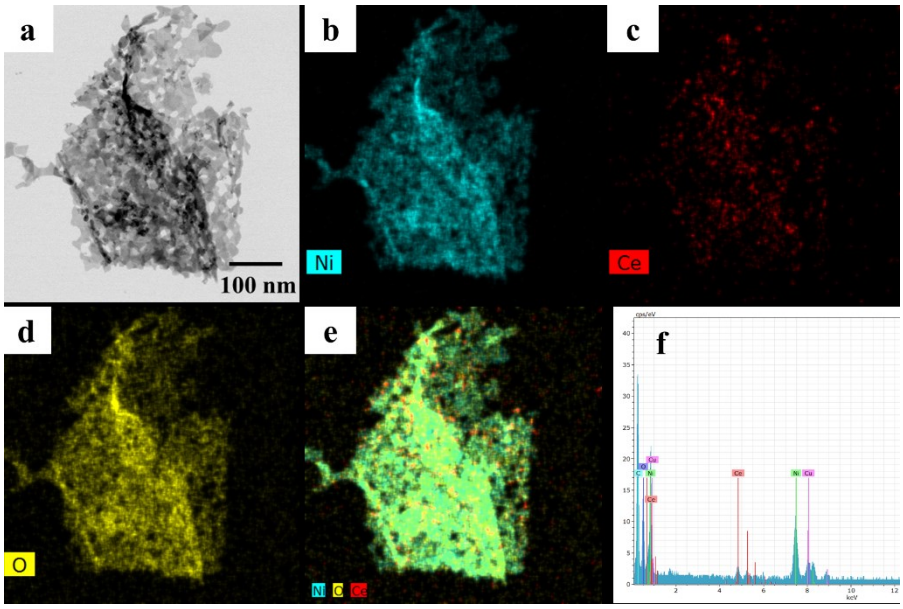

Figure 8. (a) TEM image, (b-e) elemental mappings and EDX spectrum collected from the 0.2Ce-5NiO sample.

3.3 X-ray diffraction and N_2 physisorption

X-ray diffraction analysis was used for identifying the crystal structures of the prepared NiO nanoarray catalysts. In Fig. 9a, most of the strong peaks can be ascribed to the cordierite Mg_2 ($Al_4Si_5O_{18}$) (JCPDS 01-082-1541) with an orthorhombic structure.With a slow scanning (2θ=0.004 $°s^{-1}$) during the XRD analysis in a focused 2θ range (35-45° and 61-65°), peaks corresponding to NiO can be resolved as shown in Figs. 9 b and c. The resolved peaks at 2θ = 37.4°, 43.2° and 62.8° after integrating the NiO nanoarray onto the cordierite substrate can be assigned to the {111}, {200} and {220} crystal planes of cubic NiO (JCPDF 073-1523). Moreover, no obvious peaks related to ceria are observed even with a higher Ce doping in the NiO, suggesting the successful doping of Ce into NiO crystal structure.

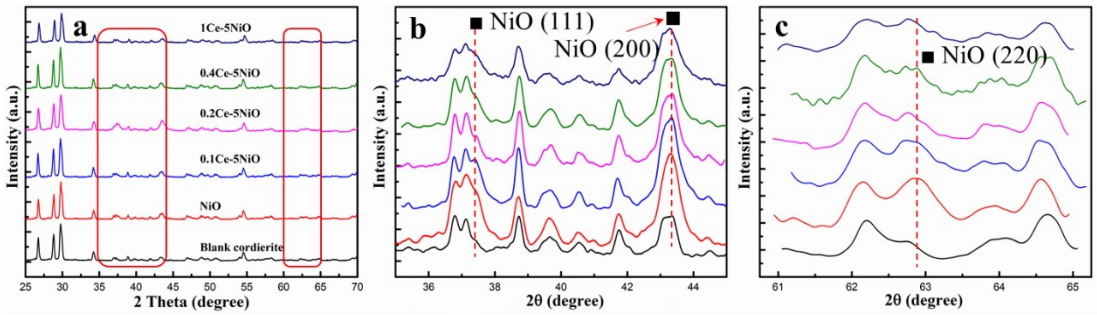

Figure 9. XRD patterns of the blank cordierite and Ce doped NiO array catalysts. (a) 25-70 °, (b) 35-45 ° and (c) 61-65 °.

Fig. 10 shows the nitrogen adsorption-desorption isotherms and pore size distribution of NiO nanoarray based monoliths with different doping concentrations of cerium. All adsorption-desorption curves exhibit a clear hysteresis loop with type IV characteristic, which usually corresponds to macro- and mesoporous structures of the catalysts. From the morphology analysis, it can be seen that the macroporous structure is from the array structure where the nanosheet array were assembled with uniform sub-micrometer pore distribution. Meanwhile, the mesoporous structure can be ascribed to the abundant pores observed on the individual nanosheets as revealed in the STEM analysis (Figs. 7 and 8). With cerium doping, the adsorption-desorption characteristic is kept well while the pore distribution has changed evidently. For pure NiO, the pore size is concentrated on about 21.7 nm as listed in Table 1. It is

noticeable that the pore size distribution becomes wider when the cerium was introduced into the arrays, demonstrating the metal components in the precursor have a great effect on the formation of irregular pores during the decomposition. As displayed in Table 1, the surface areas of all samples are at the range of 4.0-5.0 m^2g^{-1}. The average pore size of Ce doped NiO became bigger (30.9-36.6 nm) except the 1Ce-5NiO sample with a poor array morphology, which is consistent with the result obtained from STEM analysis. For 1Ce-5NiO, the array structure almost disappears, with a more-densely covered film on the surface as revealed in Fig. 4f. With higher Ce precursor concentration involved into the hydrothermal process, more cerium-derived precipitates formed and induce the collapse of nanoarray structure. As a result, there will be more nanoparticles formed after annealing and the dense film with smaller pore size distribution will be generated with the aggregation of nanocrystals.

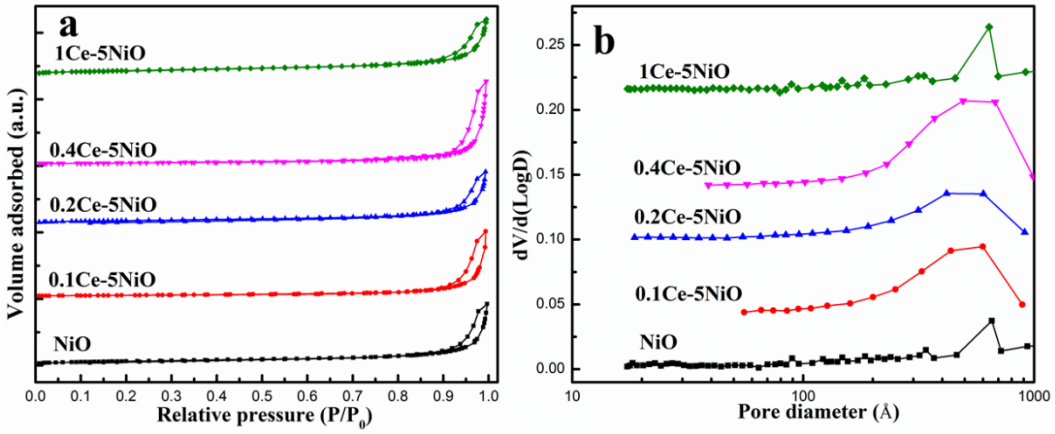

Figure 10. (a) Nitrogen adsorption-desorption isotherms and (b) BJH pore size distribution calculated from the adsorption branch of the isotherm for as-prepared Ce-Ni array catalysts.

3.4 H_2-TPR and XPS analysis

Reducibility is usually applied to explain the catalytic reactions on the NiO based catalysts [41, 42, 44, 62-64]. In this study, H_2-TPR experiments were used to investigate the reducibility of as-prepared samples. In the case of pure NiO, a main asymmetrical reduction peak is observed in Fig. 11 with a superimposed peak at higher temperature. Generally, the reduction of NiO under hydrogen atmosphere includes the processes of Ni^{3+} to Ni^{2+} and Ni^{2+} to Ni^0, where higher temperature is needed for the further reduction [41, 42, 44, 62]. After doping with cerium, the reduction peak moves to lower temperature obviously. The 0.2Ce-5Ni sample has the

best low-temperature reducibility, indicating the cerium doping can significantly promote the activity of oxygen in NiO based catalyst. However, the best promoting effect occurred at the doping amount of about 4% (0.2Ce-5Ni) on their reducibility, which was hardly further enhanced with a higher doping ratio.

The surface chemical species of two typical samples including pure NiO and 0.2Ce-5NiO were examined by XPS. As shown in Fig. S1, the clear Ce3d peak on the sample 0.2Ce-5NiO confirms the presence of Ce species in the Ce doped sample. With Ce doping, the splitting peak of Ni2p around 852.0-856.0 eV becomes non-obvious, shown in Fig. S2. This indicates the doped Ce has a significant effect on the distribution of Ni species on the surface. For spectra of O1s, the peak at higher binding energy is generally ascribed to the surface adsorbed oxygens, which play a vital role in catalytic oxidation process [45, 60, 65-69]. As a result, the peak at higher binding energy becomes much stronger after Ce doping, which confirms the doping Ce of NiO can enhance the distribution of surface active oxygen species.

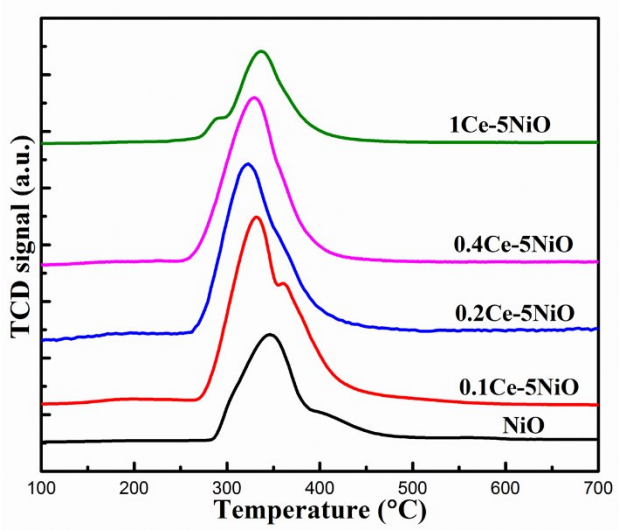

Figure 11. H_2-TPR profiles of the Ce doped NiO nanoarray catalysts.

3.5 Discussions

Our previously studies have pointed out that ordered 3D nanostructures in the nanoarray based monolithic catalysts can provide an excellent physical environment for mass transfer during the reactions and greatly promote the catalytic activities with high material utilization efficiency [11, 13-15, 59, 61, 70]. In this work, we successfully fabricated the NiO nanosheet array based monolithic catalysts, which can be effectively utilized for catalytic combustion of propane. As shown in Fig. 4, all

nanosheets are inter-connected to enclose numerous sub-micrometer spaces passing through the whole array layer. TEM analysis reveals a number of mesopores on every single nanosheet, making every nanometer spaces enclosed by nanosheets be interconnected. For traditional washcoat based catalysts, it is a critical issue for internal mass transfer in the thick (20-200 μm) and dense layer with random pores [71-74], and this kind of diffusional limitations can play a vital role in determining the catalytic behavior of monoliths. Moreover, due to the micrometer thickness of NiO nanoarray, the catalyst material usage on our monolithic catalyst is only 26.8 g L^{-1}, which is 5-14 times lower than the loading of washcoat catalyst (150-350 g L^{-1}) [75-79], further demonstrating its ultra-high material utilization efficiency.

With cerium doping, the catalytic performance of NiO based monolithic catalyst is significantly enhanced while maintaining the array structures. It should be noted that the stability of Ce-doped NiO catalyst is significantly improved upon that of the pristine NiO. From the XRD data, no peaks of ceria phase were observed due to the high intensity background from cordierite crystal structure, it is still difficult to accurately determine the cerium incorporated into the cubic nickel oxide. However, considering the size of Ce and Ni, the replacement of Ce ions into the NiO lattice site is highly possible, as reported by other studies [32, 80, 81]. Meanwhile, the compositional analysis using EDXS revealed a homogeneous distribution of Ni and Ce throughout the catalysts, proving the successful incorporation of Ce into NiO. The doping content of Ce into NiO is limited due to the difference of their ion size and electric charge. For example, in the sample 1Ce-5Ni, the morphology of nanosheet unit was not kept well due to the formation of additional cerium oxide. Significant phase segregation is expected due to large lattice strain and compression resulted from cerium incorporation [80, 82-84], with the much larger ionic radii in Ce^{3+} and Ce^{4+} (1.15 and 1.01 Å, respectively) compared to 0.83 Å in Ni^{2+}. As shown in TPR analysis, the reducibility of Ce doped NiO catalysts was clearly improved at the lower temperature zone, which is highly related to the boosted low-temperature catalytic activities, indicating the significantly promoted activity of bonded oxygen species due to Ce doping.

4. Conclusions

In summary, we have successfully integrated NiO based nanosheet array onto the channel surfaces of cordierite honeycomb to form a robust monolithic catalyst with

ultra-low loading for catalytic propane combustion. The low-temperature oxidation activities of NiO nanosheet array based catalyst can be markedly promoted by the Ce doping with well-retained array structure. The Ce-doped NiO exhibits much better stability than the pristine counterpart. It is suggested that the interaction between Ce and Ni improves the low temperature reducibility of NiO, further promoting the catalyst reactivity and stability significantly. This work provides a new design of PGM free nanoarray based monolithic catalysts with ultra-low material loading for efficient and robust hydrocarbon combustion.

Acknowledgements

The authors are grateful for the financial support from the US Department of Energy (Award No. DE-EE0006854) and the US National Science Foundation (Award Nos. CBET-1344792 and IIP-1919231).

References

[1] R.M. Heck, S. Gulati, R.J. Farrauto, The application of monoliths for gas phase catalytic reactions, Chemical Engineering Journal, 82 (2001) 149-156.
[2] P. Avila, M. Montes, E.E. Miro, Monolithic reactors for environmental applications: A review on preparation technologies, Chem. Eng. J., 109 (2005) 11-36.
[3] S. Irandoust, B. Andersson, Monolithic catalysts for nonautomobile applications, Catalysis Reviews Science and Engineering, 30 (1988) 341-392.
[4] S.G. Lehman, L. Liu, Application of ceramic membranes with pre-ozonation for treatment of secondary wastewater effluent, Water Research, 43 (2009) 2020-2028.
[5] T. Boger, A.K. Heibel, C.M. Sorensen, Monolithic catalysts for the chemical industry, Industrial & Engineering Chemistry Research, 43 (2004) 4602-4611.
[6] W.M. Carty, P.W. Lednor, Monolithic ceramics and heterogeneous catalysts: honeycombs and foams, Current Opinion in Solid State and Materials Science, 1 (1996) 88-95.
[7] T. Nijhuis, M. Kreutzer, A. Romijn, F. Kapteijn, J. Moulijn, Monolithic catalysts as efficient three-phase reactors, Chemical Engineering Science, 56 (2001) 823-829.
[8] R.J. Farrauto, R.M. Heck, Catalytic converters: state of the art and perspectives, Catalysis Today, 51 (1999) 351-360.
[9] A.K. Neyestanaki, F. Klingstedt, T. Salmi, D.Y. Murzin, Deactivation of postcombustion catalysts, a review, Fuel, 83 (2004) 395-408.
[10] S.i. Matsumoto, Recent advances in automobile exhaust catalysts, Catalysis Today, 90 (2004) 183-190.
[11] Y. Guo, Z. Ren, W. Xiao, C. Liu, H. Sharma, H. Gao, A. Mhadeshwar, P.-X. Gao, Robust 3-D configurated metal oxide nano-array based monolithic catalysts with ultrahigh materials usage efficiency and catalytic performance tunability, Nano Energy, 2 (2013) 873-881.
[12] Z. Ren, Z. Wu, W. Song, W. Xiao, Y. Guo, J. Ding, S.L. Suib, P.-X. Gao, Low temperature propane oxidation over Co 3 O 4 based nano-array catalysts: Ni dopant effect, reaction mechanism and structural stability, Applied Catalysis B: Environmental, 180 (2016) 150-160.
[13] S.-Y. Chen, W. Song, H.-J. Lin, S. Wang, S. Biswas, M. Mollahosseini, C.-H. Kuo, P.-X. Gao, S.L. Suib, Manganese Oxide Nano-Array Based Monolithic Catalysts: Tunable Morphology and High Efficiency for CO Oxidation, ACS Appl. Mater. Interfaces, (2016).
[14] Z. Ren, V. Botu, S. Wang, Y. Meng, W. Song, Y. Guo, R. Ramprasad, S.L. Suib, P.X. Gao,

Monolithically integrated spinel MxCo3− xO4 (M= Co, Ni, Zn) nanoarray catalysts: scalable synthesis and cation manipulation for tunable low‐temperature CH4 and CO oxidation, Angewandte Chemie International Edition, 53 (2014) 7223-7227.
[15] S. Wang, Z. Ren, Y. Guo, P.-X. Gao, Nano-array integrated monolithic devices: toward rational materials design and multi-functional performance by scalable nanostructures assembly, CrystEngComm, 18 (2016) 2980-2993.
[16] S. Wang, Z. Ren, W. Song, Y. Guo, M. Zhang, S.L. Suib, P.-X. Gao, ZnO/perovskite core–shell nanorod array based monolithic catalysts with enhanced propane oxidation and material utilization efficiency at low temperature, Catal. Today, 258 (2015) 549-555.
[17] W. Tang, X. Lu, F. Liu, S. Du, J. Weng, S. Hoang, S. Wang, C.-Y. Nam, P.-X. Gao, Ceria-based nanoflake arrays integrated on 3D cordierite honeycombs for efficient low-temperature diesel oxidation catalyst, Applied Catalysis B: Environmental, 245 (2019) 623-634.
[18] S.-Y. Chen, W. Tang, J. He, R. Miao, H.-J. Lin, W. Song, S. Wang, P.-X. Gao, Steven L. Suib, Copper manganese oxide enhanced nanoarray-based monolithic catalysts for hydrocarbon oxidation, Journal of Materials Chemistry A, 6 (2018) 19047-19057.
[19] X. Lu, W. Tang, S. Du, L. Wen, J. Weng, Y. Ding, W.S. Willis, S.L. Suib, P.-X. Gao, Ion-Exchange Loading Promoted Stability of Platinum Catalysts Supported on Layered Protonated Titanate-Derived Titania Nanoarrays, ACS applied materials & interfaces, 11 (2019) 21515-21525.
[20] P. Gélin, M. Primet, Complete oxidation of methane at low temperature over noble metal based catalysts: a review, Applied Catalysis B: Environmental, 39 (2002) 1-37.
[21] T.P. Kobylinski, B.W. Taylor, The catalytic chemistry of nitric oxide: II. Reduction of nitric oxide over noble metal catalysts, Journal of Catalysis, 33 (1974) 376-384.
[22] T.V. Johnson, Review of diesel emissions and control, International Journal of Engine Research, 10 (2009) 275-285.
[23] Y. Luo, J. Zuo, X. Feng, Q. Qian, Y. Zheng, D. Lin, B. Huang, Q. Chen, Good interaction between well dispersed Pt and LaCoO3 nanorods achieved rapid Co3+/Co2+ redox cycle for total propane oxidation, Chemical Engineering Journal, 357 (2019) 395-403.
[24] J. Dunleavy, Sulfur as a catalyst poison, Platinum Metals Review, 50 (2006) 110.
[25] N. Bion, F. Epron, M. Moreno, F. Mariño, D. Duprez, Preferential oxidation of carbon monoxide in the presence of hydrogen (PROX) over noble metals and transition metal oxides: advantages and drawbacks, Topics in Catalysis, 51 (2008) 76.
[26] H. Gandhi, M. Shelef, Effects of sulphur on noble metal automotive catalysts, Applied Catalysis, 77 (1991) 175-186.
[27] H. Arai, T. Yamada, K. Eguchi, T. Seiyama, Catalytic combustion of methane over various perovskite-type oxides, Applied Catalysis, 26 (1986) 265-276.
[28] W. Li, J. Wang, H. Gong, Catalytic combustion of VOCs on non-noble metal catalysts, Catal. Today, 148 (2009) 81-87.
[29] S.C. Kim, The catalytic oxidation of aromatic hydrocarbons over supported metal oxide, Journal of Hazardous materials, 91 (2002) 285-299.
[30] L. Chen, J. Ding, J. Jia, R. Ran, C. Zhang, X. Song, Cobalt-doped MnO2 Nanofibers for Enhanced Propane Oxidation, ACS Applied Nano Materials, (2019).
[31] Z. Hu, S. Qiu, Y. You, Y. Guo, Y. Guo, L. Wang, W. Zhan, G. Lu, Hydrothermal synthesis of NiCeOx nanosheets and its application to the total oxidation of propane, Applied Catalysis B: Environmental, 225 (2018) 110-120.
[32] S.R. Gawali, D.P. Dubal, V.G. Deonikar, S.S. Patil, S.D. Patil, P. Gomez-Romero, D.R. Patil, J. Pant, Asymmetric Supercapacitor Based on Nanostructured Ce-doped NiO (Ce:NiO) as Positive and Reduced Graphene Oxide (rGO) as Negative Electrode, ChemistrySelect, 1 (2016) 3471-3478.
[33] Y. Guo, G. Liu, Z. Ren, A. Piyadasa, P.-X. Gao, Single crystalline brookite titanium dioxide nanorod arrays rooted on ceramic monoliths: a hybrid nanocatalyst support with ultra-high surface area and thermal stability, CrystEngComm, 15 (2013) 8345-8352.
[34] S. Du, W. Tang, X. Lu, S. Wang, Y. Guo, P.X. Gao, Cu‐Decorated ZnO Nanorod Array Integrated Structured Catalysts for Low‐Pressure CO2 Hydrogenation to Methanol, Advanced Materials Interfaces, 5 (2018) 1700730.
[35] W. Tang, Z. Ren, X. Lu, S. Wang, Y. Guo, S. Hoang, S. Du, P.X. Gao, Scalable Integration of Highly Uniform MnxCo3− xO4 Nanosheet Array onto Ceramic Monolithic Substrates for Low‐Temperature Propane Oxidation, ChemCatChem, 9 (2017) 4112-4119.

[36] W. Tang, S. Wang, W. Xiao, S. Du, X. Lu, S. Hoang, J. Ding, P.-X. Gao, Pre-surface leached cordierite honeycombs for MnxCo3-xO4 nano-sheet array integration with enhanced hydrocarbons combustion, Catalysis Today, 320 (2019) 196-203.
[37] S. Hoang, X. Lu, W. Tang, S. Wang, S. Du, C.-Y. Nam, Y. Ding, R.D. Vinluan, J. Zheng, P.-X. Gao, High performance diesel oxidation catalysts using ultra-low Pt loading on titania nanowire array integrated cordierite honeycombs, Catalysis Today, 320 (2019) 2-10.
[38] J. He, S.-Y. Chen, W. Tang, Y. Dang, P. Kerns, R. Miao, B. Dutta, P.-X. Gao, S.L. Suib, Microwave-assisted integration of transition metal oxide nanocoatings on manganese oxide nanoarray monoliths for low temperature CO oxidation, Applied Catalysis B: Environmental, 255 (2019) 117766.
[39] X. Lu, S. Hoang, W. Tang, S. Du, S. Wang, F. Liu, W. Zhong, S.L. Suib, G. Yang, F.-Y. Zhang, P.-X. Gao, Direct Synthesis of Conformal Layered Protonated Titanate Nanoarray Coatings on Various Substrate Surfaces Boosted by Low-Temperature Microwave-Assisted Hydrothermal Synthesis, ACS applied materials & interfaces, 10 (2018) 35164-35174.
[40] B. Zhao, X.-K. Ke, J.-H. Bao, C.-L. Wang, L. Dong, Y.-W. Chen, H.-L. Chen, Synthesis of flower-like NiO and effects of morphology on its catalytic properties, The Journal of Physical Chemistry C, 113 (2009) 14440-14447.
[41] S. Mahammadunnisa, P.M.K. Reddy, N. Lingaiah, C. Subrahmanyam, NiO/Ce 1− x Ni x O 2− δ as an alternative to noble metal catalysts for CO oxidation, Catalysis Science & Technology, 3 (2013) 730-736.
[42] G. Bai, H. Dai, J. Deng, Y. Liu, K. Ji, Porous NiO nanoflowers and nanourchins: highly active catalysts for toluene combustion, Catal. Commun., 27 (2012) 148-153.
[43] M.-G. Jeong, E.J. Park, B. Jeong, D.H. Kim, Y.D. Kim, Toluene combustion over NiO nanoparticles on mesoporous SiO 2 prepared by atomic layer deposition, Chemical Engineering Journal, 237 (2014) 62-69.
[44] W. Tang, Y. Deng, W. Li, S. Li, X. Wu, Y. Chen, Restrictive nanoreactor for growth of transition metal oxides (MnO 2, Co 3 O 4, NiO) nanocrystal with enhanced catalytic oxidation activity, Catalysis Communications, 72 (2015) 165-169.
[45] W. Tang, Y. Deng, W. Li, J. Li, G. Liu, S. Li, X. Wu, Y. Chen, Importance of porous structure and synergistic effect on the catalytic oxidation activities over hierarchical Mn–Ni composite oxides, Catalysis Science & Technology, 6 (2016) 1710-1718.
[46] B. Dhandapani, S.T. Oyama, Gas phase ozone decomposition catalysts, Applied Catalysis B: Environmental, 11 (1997) 129-166.
[47] M. Stoyanova, P. Konova, P. Nikolov, A. Naydenov, D. Mehandjiev, Alumina-supported nickel oxide for ozone decomposition and catalytic ozonation of CO and VOCs, Chemical Engineering Journal, 122 (2006) 41-46.
[48] N. Pasha, N. Lingaiah, P.S.S. Reddy, P.S. Prasad, An investigation into the effect of Cs promotion on the catalytic activity of NiO in the direct decomposition of N2O, Catalysis Letters, 118 (2007) 64-68.
[49] I.D. Gay, Catalytic decomposition of N2O and oxygen desorption spectra on NiO, Journal of Catalysis, 17 (1970) 245-251.
[50] Y. Wang, A. Zhu, Y. Zhang, C. Au, X. Yang, C. Shi, Catalytic reduction of NO by CO over NiO/CeO 2 catalyst in stoichiometric NO/CO and NO/CO/O 2 reaction, Applied Catalysis B: Environmental, 81 (2008) 141-149.
[51] Y. Wan, W. Zhao, Y. Tang, L. Li, H. Wang, Y. Cui, J. Gu, Y. Li, J. Shi, Ni-Mn bi-metal oxide catalysts for the low temperature SCR removal of NO with NH 3, Applied Catalysis B: Environmental, 148 (2014) 114-122.
[52] C.-C. Hu, H. Teng, Structural features of p-type semiconducting NiO as a co-catalyst for photocatalytic water splitting, Journal of Catalysis, 272 (2010) 1-8.
[53] R.D. Smith, M.S. Prévot, R.D. Fagan, Z. Zhang, P.A. Sedach, M.K.J. Siu, S. Trudel, C.P. Berlinguette, Photochemical route for accessing amorphous metal oxide materials for water oxidation catalysis, Science, 340 (2013) 60-63.
[54] A. Singh, S.L. Chang, R.K. Hocking, U. Bach, L. Spiccia, Anodic deposition of NiO x water oxidation catalysts from macrocyclic nickel (ii) complexes, Catalysis Science & Technology, 3 (2013) 1725-1732.
[55] J. Zhu, X. Peng, L. Yao, X. Deng, H. Dong, D. Tong, C. Hu, Synthesis gas production from CO 2 reforming of methane over Ni–Ce/SiO 2 catalyst: the effect of calcination ambience, International Journal of Hydrogen Energy, 38 (2013) 117-126.
[56] Y. Kobayashi, J. Horiguchi, S. Kobayashi, Y. Yamazaki, K. Omata, D. Nagao, M. Konno, M. Yamada, Effect of NiO content in mesoporous NiO–Al 2 O 3 catalysts for high pressure partial oxidation of

methane to syngas, Appl. Catal., A, 395 (2011) 129-137.
[57] P. Pal, R.K. Singha, A. Saha, R. Bal, A.B. Panda, Defect-induced efficient partial oxidation of methane over nonstoichiometric Ni/CeO2 nanocrystals, The Journal of Physical Chemistry C, 119 (2015) 13610-13618.
[58] L. Xu, H. Song, L. Chou, Carbon dioxide reforming of methane over ordered mesoporous NiO–MgO–Al 2 O 3 composite oxides, Applied Catalysis B: Environmental, 108 (2011) 177-190.
[59] Z. Ren, Y. Guo, Z. Zhang, C. Liu, P.-X. Gao, Nonprecious catalytic honeycombs structured with three dimensional hierarchical Co3O4 nano-arrays for high performance nitric oxide oxidation, J. Mater. Chem. A, 1 (2013) 9897-9906.
[60] Z. Zhu, G. Lu, Z. Zhang, Y. Guo, Y. Guo, Y. Wang, Highly Active and Stable Co3O4/ZSM-5 Catalyst for Propane Oxidation: Effect of the Preparation Method, ACS Catalysis, 3 (2013) 1154-1164.
[61] Z. Ren, Z. Wu, W. Song, W. Xiao, Y. Guo, J. Ding, S.L. Suib, P.-X. Gao, Low temperature propane oxidation over Co3O4 based nano-array catalysts: Ni dopant effect, reaction mechanism and structural stability, Applied Catalysis B: Environmental, 180 (2016) 150-160.
[62] J. Rynkowski, T. Paryjczak, M. Lenik, On the nature of oxidic nickel phases in NiO/γ-Al 2 O 3 catalysts, Applied Catalysis A: General, 106 (1993) 73-82.
[63] H. Mori, C.-j. Wen, J. Otomo, K. Eguchi, H. Takahashi, Investigation of the interaction between NiO and yttria-stabilized zirconia (YSZ) in the NiO/YSZ composite by temperature-programmed reduction technique, Applied Catalysis A: General, 245 (2003) 79-85.
[64] B. Mile, D. Stirling, M.A. Zammitt, A. Lovell, M. Webb, The location of nickel oxide and nickel in silica-supported catalysts: two forms of "NiO" and the assignment of temperature-programmed reduction profiles, Journal of Catalysis, 114 (1988) 217-229.
[65] K. Ji, H. Dai, J. Deng, L. Song, B. Gao, Y. Wang, X. Li, Three-dimensionally ordered macroporous Eu0.6Sr0.4FeO3 supported cobalt oxides: Highly active nanocatalysts for the combustion of toluene, Applied Catalysis B: Environmental, 129 (2013) 539-548.
[66] W. Tang, W. Li, D. Li, G. Liu, X. Wu, Y. Chen, Synergistic Effects in Porous Mn–Co Mixed Oxide Nanorods Enhance Catalytic Deep Oxidation of Benzene, Catal. Lett., 144 (2014) 1900-1910.
[67] Y. Zhang, Z. Qin, G. Wang, H. Zhu, M. Dong, S. Li, Z. Wu, Z. Li, Z. Wu, J. Zhang, T. Hu, W. Fan, J. Wang, Catalytic performance of MnOx–NiO composite oxide in lean methane combustion at low temperature, Applied Catalysis B: Environmental, 129 (2013) 172-181.
[68] W. Tang, J. Li, X. Wu, Y. Chen, Limited nanospace for growth of Ni–Mn composite oxide nanocrystals with enhanced catalytic activity for deep oxidation of benzene, Catalysis Today, 258 (2015) 148-155.
[69] Y. Deng, W. Tang, W. Li, Y. Chen, MnO2-nanowire@ NiO-nanosheet core-shell hybrid nanostructure derived interfacial Effect for promoting catalytic oxidation activity, Catalysis Today, 308 (2018) 58-63.
[70] Z. Ren, Y. Guo, P.-X. Gao, Nano-array based monolithic catalysts: Concept, rational materials design and tunable catalytic performance, Catalysis Today, 258 (2015) 441-453.
[71] R. Hayes, B. Liu, R. Moxom, M. Votsmeier, The effect of washcoat geometry on mass transfer in monolith reactors, Chem. Eng. Sci., 59 (2004) 3169-3181.
[72] M. Bhattacharya, M.P. Harold, V. Balakotaiah, Mass‐transfer coefficients in washcoated monoliths, AIChE Journal, 50 (2004) 2939-2955.
[73] S.Y. Joshi, M.P. Harold, V. Balakotaiah, Overall mass transfer coefficients and controlling regimes in catalytic monoliths, Chem. Eng. Sci., 65 (2010) 1729-1747.
[74] S.Y. Joshi, M.P. Harold, V. Balakotaiah, On the use of internal mass transfer coefficients in modeling of diffusion and reaction in catalytic monoliths, Chem. Eng. Sci., 64 (2009) 4976-4991.
[75] T.J. Toops, B.G. Bunting, K. Nguyen, A. Gopinath, Effect of engine-based thermal aging on surface morphology and performance of Lean NO x Traps, Catalysis Today, 123 (2007) 285-292.
[76] M. Han, D.N. Assanis, S.V. Bohac, Comparison of HC species from diesel combustion modes and characterization of a heat-up doc formulation, International Journal of Automotive Technology, 9 (2008) 405-413.
[77] A. Winkler, D. Ferri, R. Hauert, Influence of aging effects on the conversion efficiency of automotive exhaust gas catalysts, Catalysis Today, 155 (2010) 140-146.
[78] C. Agrafiotis, A. Tsetsekou, C. Stournaras, A. Julbe, L. Dalmazio, C. Guizard, G. Boretto, M. Debenedetti, F. Parussa, Evaluation of sol–gel methods for the synthesis of doped-ceria environmental catalysis systems: Part II. Catalytic activity and resistance to thermal aging, Applied Catalysis B: Environmental, 34 (2001) 149-159.

[79] V. Meeyoo, D. Trimm, N. Cant, The effect of sulphur containing pollutants on the oxidation activity of precious metals used in vehicle exhaust catalysts, Applied Catalysis B: Environmental, 16 (1998) L101-L104.
[80] G. Anandha babu, G. Ravi, T. Mahalingam, M. Navaneethan, M. Arivanandhan, Y. Hayakawa, Size and Surface Effects of Ce-Doped NiO and Co3O4 Nanostructures on Ferromagnetism Behavior Prepared by the Microwave Route, The Journal of Physical Chemistry C, 118 (2014) 23335-23348.
[81] S.R. Gawali, V.L. Patil, V.G. Deonikar, S.S. Patil, D.R. Patil, P.S. Patil, J. Pant, Ce doped NiO nanoparticles as selective NO 2 gas sensor, Journal of Physics and Chemistry of Solids, 114 (2018) 28-35.
[82] P. Muthukumaran, C.V. Raju, C. Sumathi, G. Ravi, D. Solairaj, P. Rameshthangam, J. Wilson, S. Rajendran, S. Alwarappan, Cerium doped nickel-oxide nanostructures for riboflavin biosensing and antibacterial applications, New Journal of Chemistry, 40 (2016) 2741-2748.
[83] A. Matsuda, S. Akiba, M. Kasahara, T. Watanabe, Y. Akita, M. Yoshimoto, Anisotropic electric conduction derived from self-organized nanogroove array on Li-doped NiO epitaxial film, Applied Physics Letters, 90 (2007) 182107.
[84] J. Ko, B.-K. Kim, J.W. Han, Density functional theory study for catalytic activation and dissociation of CO2 on bimetallic alloy surfaces, The Journal of Physical Chemistry C, 120 (2016) 3438-3447.